Physica B 666 (2023) 415090

Contents lists available at ScienceDirect

Physica B: Condensed Matter

journal homepage: www.elsevier.com/locate/physb

Structure, site symmetry and spin-orbit coupled magnetism of a $Ca_{12}Al_{14}O_{33}$ mayenite single crystal substituted with 0.26 at.% Ni

Björn Schwarz [a,*], Stefan G. Ebbinghaus [b], Andreas Eichhöfer [c], Laura Simonelli [d], Holger Krause [b], Thomas Bergfeldt [a], Sylvio Indris [a], Jürgen Janek [e], Helmut Ehrenberg [a]

[a] Institute for Applied Materials (IAM), Karlsruhe Institute of Technology (KIT), Hermann-von-Helmholtz-Platz 1, 76344, Eggenstein-Leopoldshafen, Germany
[b] Institute of Chemistry, Martin Luther University Halle-Wittenberg, Kurt-Mothes-Straße 2, 06120, Halle, Germany
[c] Institute of Nanotechnology (INT), Karlsruhe Nano Micro Facility (KNMFi), Karlsruhe Institute of Technology (KIT), Hermann-von-Helmholtz-Platz 1, 76344, Eggenstein-Leopoldshafen, Germany
[d] CELLS–ALBA Synchrotron, 08290, Cerdanyola Del Vallès, Barcelona, Spain
[e] Institute of Physical Chemsitry & Center for Materials Research, Justus Liebig University, 35392, Giessen, Germany

ARTICLE INFO

Keywords:
Mayenite
Nickel
Magnetism
Spin-orbit coupling
Crystal field
Magnetic anisotropy

ABSTRACT

A $Ca_{12}Al_{14}O_{33}$ mayenite single crystal with 0.26(1) at.% of the metals substituted by Ni was synthesized. Single crystal XRD confirms that about 10 at.% of Al and Ca partially occupy split crystallographic sites with lowered point symmetry. Ni K-edge XAS reveals that Ni is present as Ni^{2+} and substitutes Al on tetrahedral oxygen coordinated sites. UV-VIS analysis further points to the partial occupation of the trigonally distorted Al(1) and Al (1B) sites by Ni^{2+}. In accordance with the results from the analytical methods, the magnetic model consists of Ni^{2+} with spin $S = 1$ on a trigonally distorted tetrahedral coordination site. The *J*-mulitplet splitting due to spin-orbit coupling with a non-magnetic $J = 0$ ground state determines the characteristic thermomagnetic properties which show a maximum of the effective paramagnetic moment of 3.61(1) μ_B at about 191 K and an uniaxial anisotropy (crystal field parameter $B_0^2 = 69.5(2)$ cm^{-1}).

1. Introduction

Mayenites form a group of nano porous oxides based on the mineral 'mayenite' $Ca_{12}Al_{14}O_{33}$. Often the short notation C12A7 is used as its composition can formally be described as 12 $CaO \cdot 7\ Al_2O_3$. Its crystal structure consists of a positively charged $(Ca_{12}Al_{14}O_{32})^{2+}$ framework that exhibits six cage-like vacancies per unit cell. In the parent compound charge neutrality is achieved by the 33rd 'free' oxide ion (also denoted as 'cage oxygen'), which statistically occupies one of the six cages and leads to a high ionic conductivity at elevated temperature. Mayenite is therefore an interesting material for various applications including solid oxide fuel cells, oxygen gas sensors, or oxidation catalysis. The most interesting aspect about mayenite is the large variety of ions that can occupy the cage positions. Besides O^{2-}, anions like Cl^-, F^-, $(OH)^-$ [1,2], or for even more 'exotic' ions like O^- [3], H^- [4] O_2^-, or electrons e^- [5] have been reported. Several studies have been published considering the effects of cation substitution in mayenites. Substitution on the Al site by Zn and P was reported to increase the activation energy and to reduce the low temperature ionic conductivity [6] whereas for substitution by Si an improved conductivity was found [7]. Electron paramagnetic resonance was used for obtaining structural information about speciation and local environment in Cu^{2+} substituted mayenites [8]. Ir^{4+} incorporated mayenite single crystals were reported to form by Czochralski crystal growth in Ir crucibles [9]. A comparative study of oxygen transport was published for one nominally undoped, one iron-doped and one nickel-doped mayenite single crystal [10]. Single crystals of mayenite with 1 at.% of Al substituted by Fe (corresponds to ~0.54 at.% referred to all metals) were found to exhibit a slightly lowered conductivity under reducing conditions compared to the pure mayenite [11]. Further, it was reported that the Fe^{3+} ions substitute Al^{3+} on tetrahedral sites and that the magnetic properties can be explained by a spin-only $S = {}^5/_2$ with quasi free-ion behaviour.

In this work, a mayenite single crystal has been grown by the floating zone technique with a small amount of 0.26(1) at.% of the metals (predominantly Al^{3+}) substituted by paramagnetic Ni^{2+} ions. The magnetic properties are very different compared with those of the Fe

* Corresponding author. Karlsruhe Institute of Technology (KIT), Institute for Applied Materials - Energy Storage Systems (IAM-ESS), Hermann-von-Helmholtz-Platz 1, 76344, Eggenstein-Leopoldshafen, Germany.
E-mail address: bjoern.schwarz@kit.edu (B. Schwarz).

https://doi.org/10.1016/j.physb.2023.415090
Received 13 April 2023; Received in revised form 16 May 2023; Accepted 22 June 2023
Available online 29 June 2023

substituted mayenite, since for Ni^{2+} the strong orbital momentum contribution and spin-orbit coupling cause a strong deviation from a free-ion like behaviour. The chemical composition of the grown crystal has been precisely determined by ICP-OES, the crystal structure has been characterized by single crystal XRD, and the oxidation state as well as local oxygen coordination by synchrotron XAS. By UV–Vis absorption spectroscopy, more detailed information about the local oxygen coordination of the substituting Ni^{2+} was obtained. Comprehensive DC magnetometry data were fitted by a phenomenological Hamiltonian approach to extract information about the spin and orbital momentum contribution, as well as local uniaxial anisotropy. Heat capacity and electric transport measurements complete the physical property characterization of the C12A7:Ni single crystal.

2. Materials and methods

2.1. Crystal synthesis

Growth of the Ni-substituted C12A7 crystal with nominally 1 at.% of Al substituted by Ni was carried out as described in detail in Ref. [12]. In short, a polycrystalline sample was prepared by solid state synthesis at 1250 °C starting from high-purity chemicals. After milling and hydrostatical pressing to rods, crystal growth was carried out in a Crystal Systems Corporation optical floating zone furnace model FZ-T-10000-H-VPO-PC equipped with four 1000 W halogen lamps under 100 ml min^{-1} gas flow (2 % O_2/98 % N_2). To achieve high-quality crystals, a two-step crystallization was applied in which the material was first molten/crystallized with 5 mm h^{-1} followed by a second, much slower crystallization at 0.2 mm h^{-1}. The obtained crystal is denoted as C12A7:Ni throughout the manuscript. For all measurements presented in this work selected pieces were cut from the same C12A7:Ni crystal.

2.2. ICP-OES

The chemical composition was determined via inductively coupled plasma optical emission spectrometry (ICP-OES) using an iCAP 7600 DUO (Thermo-Fisher-Scientific). Three different pieces of the C12A7:Ni crystal were separately dissolved in an acidic solution with supporting heating by microwave radiation and the solutions were investigated regarding the mass fractions of the metals Al, Ca, and Ni. Standard deviations were determined from statistical analysis of the results from the three different samples.

2.3. Single crystal X-ray diffraction

Single crystal X-ray diffraction (SCXRD) data was collected using Mo $K_{\alpha1}$ radiation ($\lambda = 0.71073$ Å) generated by a micro focus sealed X-ray tube (Mo Genix 3D) with a multilayer optic on a STOE STADI Vari (Pilatus Hybrid Pixel Detector 300 K) at 180 K (Oxford Cryosystem). A small part of the C12A7:Ni crystal was ground into smaller pieces, put into perfluoroalkylether oil and a suitable crystal for SCXRD was selected. Raw intensity data were collected and treated with the STOE X-Area software, e.g. corrected for Lorentz and polarization effects. With the implemented program STOE LANA, inter frame scaling of the dataset was done as well as multi-scan absorption corrections applied by scaling of reflection intensities [13]. Using Olex2 [14] the structure was solved with the ShelXT [15] structure solution program using intrinsic phasing and refined with the ShelXL [16] package by least squares minimization. Structure images were prepared using Diamond [17]. The Ca, Al, and O atoms were refined with anisotropic displacement parameters with exception of the disordered sites Al(1B) and O(3), which were refined isotropically.

2.4. Synchrotron X-Ray absorption spectroscopy

Synchrotron X-ray absorption spectra (XAS) were obtained at the BL22-CLAESS beamline [18] (ALBA CELLS synchrotron, Barcelona, Spain) using a C12A7:Ni crystal piece of approximately 15 mg with the *a*,*b*-plane at 45° with respect to the incoming beam. The XAS spectrum was measured from 8.225 to 9.500 keV in fluorescence mode by means of a multichannel silicon drift detector. The energy scale was calibrated with a Ni metal foil standard. From the extended X-ray absorption fine structure (EXAFS) spectrum a *k*-range from 2.58 to 10 $Å^{-1}$ was selected for Fourier transformation (FT) of the k^2 weighted EXAFS oscillations. For processing, analysing and simulating the XAS data the Demeter [19] program package was used.

2.5. UV-VIS

UV–vis absorption spectrum was measured on the same C12A7:Ni crystal piece as used for XAS (see Fig. S1) on a PerkinElmer Lambda 900 spectrophotometer in reflection mode inside a Labsphere integrating sphere.

2.6. Magnetic measurements

The DC magnetic moment was measured with a physical property measurement system (PPMS) DynaCool from Quantum Design equipped with a vibrating sample magnetometer (VSM) option. For the magnetic measurements, two crystal pieces with a total weight of 29.5(1) mg were stacked on each other along identical crystallographic orientation to increase the signal and attached with polyimide tape (weight 14.5 mg) to the quartz glass paddle sample holder. The crystallographic direction <100> of the crystals was oriented parallel to the external magnetic field direction (= *z* quantization axis of the magnetic moment). For a special measurement probing the macroscopic anisotropy the crystal was rotated around 45° (see also Fig. S2 for illustrations). All measurements were performed under a ~10 Torr He 5.0 gas atmosphere. The magnetic moment vs. temperature was measured with applied external fields $\mu_0 H$ of 0.5, 1, 3, 5, 7, and 9 T. For each field, the sample was first cooled to 2 K and the magnetic moment was measured during heating in temperature settle mode from 2 to 50 K and in sweep mode with 2 K/min from 50 K to 300 K with a temperature increment of 1 K and an average measuring time of 10 s per point. The magnetic moment vs. field was measured at 1.8, 2, 4, 7, 11, 16, 22, 29, 37, 46, 75, 100, and 300 K from 0 to 9 T with a field increment of 2500 Oe (0.25 T) starting at the lowest temperature. The complete sequence of measurements for all temperature and field scans was repeated with the sample removed from the holder, i.e. only with the holder and the polyimide tape contributing as diamagnetic susceptibility χ_{holder}. The diamagnetic contribution of the atomic closed shells χ_{acs} from Al, Ca, Ni, and O was determined by the incremental method according to the values listed in Table S1 that were taken from Ref. [20]. The paramagnetic susceptibility χ_{para} stemming exclusively from localized moments as confirmed below was determined from the total measured susceptibility χ_{tot} according to

$$\chi_{para} = \chi_{tot} - \chi_{acs} - \chi_{holder} \quad (1)$$

and is set to $\chi_{para} = \chi$ in the following for convenience (see Figs. S3 and S4). The magnetic models were refined to reproduce the temperature and field scans using the program PHI [21]. Equations A 1–4 (listed in Appendix A) describe the corresponding terms of the utilized phenomenological Hamiltonian.

2.7. Heat capacity

The isobaric heat capacity C_p was measured via the relaxation method using the heat capacity option of the PPMS DynaCool (Quantum Design) under high vacuum (<10 mTorr He atmosphere). At each temperature, three measurements were performed with a 2 % relative temperature rise. An addenda measurement with a small amount of heat transfer grease Apiezon N (Sigma Aldrich) on the sample platform was

measured from 300 to 1.8 K at 49 different $\log_{10}$-separated temperatures. A sample piece with dimensions 5.13(5) × 3.34(5) × 0.72(5) mm^3 and 31.2 mg mass was first measured from 100 to 1.8 K at 40 different $\log_{10}$-separated temperatures in zero field and subsequently at the same temperatures with a magnetic field of $\mu_0 H = 7$ T perpendicular to the large basal planes. Finally, the heat capacity was measured from 100 to 300 K in 10 K steps in zero field.

2.8. Electric conductivity

Electric conductivity was measured using the PPMS electric transport option (ETO) (Quantum Design). The basal planes of the same crystal piece used for the C_P measurement (Fig. S1) were covered with conductive silver epoxy ACHESON 1415 (Plano) and contacted with Cu wires to the measuring device. The resistivity was measured via a 2-wire set up and in alternating current (AC) mode at a low frequency of 1 Hz.

3. Results and discussion

3.1. ICP-OES

The chemical composition was determined via ICP-OES for three different pieces of the crystal. Table 1 presents the obtained mass fractions for Al, Ca, and Ni together with their statistically determined standard deviations. From these mass fractions the average metal atomic concentrations c_{av} are calculated with the sum of all metals set to one. The upper/lower limit Ni concentrations c_{up}/c_{low} are determined by assuming the minimum/maximum concentration for the sum of Al and Ca on one side and maximum/minimum concentration for Ni on the other side according to their standard deviations. As a result, the Ni concentration in the samples according to the ICP-OES results is 0.26 (1) at.% referenced to the sum of all metal ions Ca, Al, and Ni. Following a substitutional approach by leaving the number of all metal atoms (Ca, Al, and Ni) at 26 per formula unit as in the 'typical mayenite' composition 12 CaO · 7 Al_2O_3═$Ca_{12}Al_{14}O_{33}$, the metal sum formula can then be written as $Ca_{12.05(2)}Al_{13.88(1)}Ni_{0.068(2)}$ (see also Table S2). From this sum formula a preference for Al substitution by Ni is indicated as will be confirmed by the results from EXAFS presented in section 3.3. We note that the experimental chemical composition is different from the nominal one $Ca_{12}Al_{13.86}Ni_{0.14}O_{33}$, i.e. less Ni than expected is found in the crystal. This indicates that the partition coefficient of nickel between the melt and the solid C12A7 is significantly different from unity, in contrast to one of iron [11].

3.2. Single crystal X-ray diffraction

C12A7:Ni crystallizes in cubic $I\bar{4}3d$ symmetry (space group no. 220) with cell parameter $a = 11.9799(6)$ Å at 180 K. Table 2 lists cell parameters for a selection of mayenite single crystals and powders as given in literature for comparison. The measured lattice parameter a is the smallest in the list and closest to that measured for $Ca_{12}Al_{14}O_{33}$ at 50 K by neutron powder diffraction (NPD). Due to a positive temperature expansion coefficient the lattice parameters reported for room temperature have increased to about 11.989 Å. Furthermore, metal substitution by Ga or Fe as well as small partial oxygen substitution by free electrons (electride) also cause a slight increase of the lattice parameter. Overall, the effect of Ni substitution on the lattice parameter cannot be discriminated from the thermal expansion effects that are present simultaneously. The structural analysis of the C12A7:Ni reproduces the findings of Ebbinghaus et al. and Sakakura et al. (see Table 2). Refinement of the main electron density peaks results in a sum formula $Ca_{12}Al_{14}O_{32}$. These atoms form a cage structure in which the Al^{3+} ions Al(1) (.3. site symmetry) and Al(2) ($\bar{4}$.. site symmetry) are (distorted) tetrahedrally surrounded by four oxygen ions (see also Table 3) and at first glance each Ca^{2+} ion Ca(1) is coordinated by six oxygen ions in a distorted trigonal pyramidal fashion [22] (Fig. 1). As reported by Ebbinghaus et al. [22] and others, about 10 % of the Ca^{2+} ions Ca(1) and also about 10 % of the Al^{3+} ions Al(1) reveal a static site disorder with additional sites Ca(1B) and Al(1B), respectively. The additional Al(1B) site with triclinic/pseudo trigonal point symmetry corresponds to occupation of neighbouring oxygen tetrahedra. The 33rd oxygen that is required for charge neutrality is reported to be disordered/dislocated in the cages in proximity to the Ca^{2+} ions. Similar to the findings of Ebbinghaus et al. for pure $Ca_{12}Al_{14}O_{33}$, it was refined for the C12A7:Ni crystal as O(3) on general site 48*e* forming a 'distorted capped quadratic pyramidal' coordination polyhedron around each Ca(1B) ion. Upon the additional refinement of O(3), the R_1 drops from 2.16 to 2.04 % and wR_2 from 5.58 to 5.09 %. However, the localization and assignment of the disordered 33rd oxygen O(3) atom is somewhat ambiguous in view of its disorder and the expected low electron density (site occupation factor only 2/48 = 0.0417). Inspection of the displacement factors reveal an increased value with respect to the other oxygen ions, which might be indicative for a lower site occupation factor. Free refinement of the site occupation factor indicated a reduced value of 0.03114 leading to an overall content of oxygen of 32.747 instead of 33. Considering the abovementioned ambiguity about the refined 33rd oxygen, the oxygen content of the C12A7:Ni can be described as 33−δ with a small oxygen deficiency ~0 < δ < ~0.25 considering these ambiguities. Together with the metal ratios as determined by ICP-OES this leads to the sum formula $Ca_{12.05(2)}Al_{13.88(1)}Ni_{0.068(2)}O_{33-\delta}$. No specific information can be extracted about the Ni positions from SCXRD due to its very low concentration.

Table 1
Average metal contents and standard deviations as determined by ICP-OES for three crystal pieces of C12A7:Ni. Standard deviations are statistically determined from the results of the three samples. c_{av}, c_{low} and c_{up} are the average and the lower and upper limit atomic concentrations with the sum of all metals set equal to one.

element	avg. cont. (wt.%)	stand. dev. (wt. %)	molar mass (g/mol)	c_{av}	c_{low}	c_{up}
Al	26.7	0.1	26.98154	0.53411	0.53368	0.53455
Ca	34.4	0.2	40.07800	0.46328	0.46385	0.46270
Ni	0.284	0.014	58.69340	0.00261	0.00247	0.00275

3.3. Synchrotron X-Ray absorption spectroscopy

Ni–K edge near edge absorption (XANES) and extended X-ray absorption fine structure spectrum of good quality have been measured to access the Ni local electronic properties and structure. Ni XANES is shown in Fig. 2a for C12A7:Ni together with a reference spectrum of NiO [29] with octahedral Ni–O coordination (space group $Fm\bar{3}m$, no. 225). The much stronger pre-edge peak of Ni in C12A7:Ni at around 8332.5 eV is explained by the non-centrosymmetric tetrahedral coordination with much stronger *p-d* intermixing, enabling normally forbidden *s-d* transitions as compared with the octahedral (centrosymmetric) coordination of Ni in NiO. The energy positions of the pre-edge of C12A7:Ni and the absorption edge itself are very similar to those of NiO indicating that nickel is present as Ni^{2+} in C12Al7:Ni. While NiO shows a pronounced white line at about 8350 eV, the C12A7:Ni crystal present two main peaks at slightly higher and lower energies indicating a different local geometry. The Fourier transform (FT) of the k^2 weighted EXAFS oscillations (Fig. 2b) shows two main features that can be ascribed to the Ni–O and Ni–Ca/Al first coordination shells, respectively. Simple single scattering path EXAFS FTs were simulated (and rescaled in intensity) for the $Ca_{12}Al_{14}O_{33}$ structure as determined by SCXRD for Ni positioned on either an Al(2) (very similar results were obtained for Al (1)) or on the Ca(1) site, respectively, considering only the nearest oxygen and Ca/Al atoms as defined in Table S3. From the comparison of the experimental

Table 2
Composition, lattice parameter *a*, total number of Ca and Al crystallographic sites, applied analytical method and the measuring temperature for various mayenites. [a] SCXRD: single crystal X-Ray diffraction, SCSRD: single crystal synchrotron radiation diffraction, NPD: neutron powder diffraction, PXRD: powder X-ray diffraction. [b] rt: room temperature.

Reference	composition	lattice parameter *a* (Å)	2 Ca sites	3 Al sites	method[a]	temp. (K)[b]
Bartl et al. [23]	$Ca_{12}Al_{14}O_{33}$	11.989(1)	–	–	SCXRD	rt
Ebbinghaus et al. [22]	$Ca_{12}Al_{14}O_{33}$	11.9883(4)	yes	yes	SCXRD	rt
Sakakura et al. [24]	$Ca_{12}Al_{14}O_{33}$	11.989(3)	yes	yes	SCSRD	298
Kiyanagi et al. [25]	$Ca_{12}Al_{14}O_{33}$	11.98127(2)	yes	no	NPD	50
Boysen et al. [26]	$Ca_{12}Al_{14}O_{33}$	11.9794	yes	no	NPD	298
		12.0308	yes	no	NPD	973
Palacios et al. [27]	$Ca_{12}Al_{13}GaO_{33}$	11.99734(6)	yes	no	PXRD/NPD	rt
Ebbinghaus et al. [11]	$Ca_{12}Al_{14}O_{33}$ with 1 mol %	11.9904(4)	–	–	PXRD	rt
Palacios et al. [28]	$Ca_{12}Al_{14}O_{33}$	11.98681(1)	yes	no	PXRD/NPD	rt
	$Ca_{12}Al_{14}O_{32.5}$	11.99215(1)	yes	no	PXRD/NPD	rt
Matsuishi et al. [5]	$Ca_{12}Al_{14}O_{32}$	11.998560(13)	no	no	PXRD	rt
		12.00472(24)	no		NPD	rt
this work	$Ca_{12.05}Al_{13.88}Ni_{0.068}O_{33-\delta}$	11.9799(6)	yes	yes	SCXRD	180

Table 3
Al–O and Ca–O coordination polyhedra for various sites according to the refined structural data from SCXRD obtained for the C12A7:Ni crystal. [a] site occupancy factor, [b] site occupancy factor 2/48 = 0.0417 on the 48*e* site.

site symmetry	central atom (Wyck., s.o.f.[a])	coordination	distance (Å)
1. ideal tetrahedron ($\bar{4}$..)	Al(2) (12*b*, 1)	4·O(1)	1.7390 (13)
2. trigonal distorted tetrahedron (.3.)	Al(1) (16*c*, 0.9)	3·O(1)	1.7797 (14)
		1·O(2)	1.725 (2)
3. triclinic distorted tetrahedron (1)	Al(1B) (48*e*, 0.0333)	O(1)	1.850 (14)
that is quasi trigonally distorted		O(1)	1.689 (16)
		O(2)	1.687 (15)
		O(3)[b]	1.67 (4)
4. monoclinic distorted trigonal bi-prism (2..)	Ca(1) (24*d*, 0.869)	2·O(1)	2.3447 (13)
		2·O(1)	2.5132 (18
		2·O(2)	2.4164 (11)
5. monoclinic distorted capped quadratic pyramid (2..)	Ca(1B) (24*d*, 0.131)	2·O(1)	2.396 (4)
		2·O(2)	2.3539 (10)
		2·O(3)[b]	2.16 (4)
		2·O(3)[b]	2.50 (4)

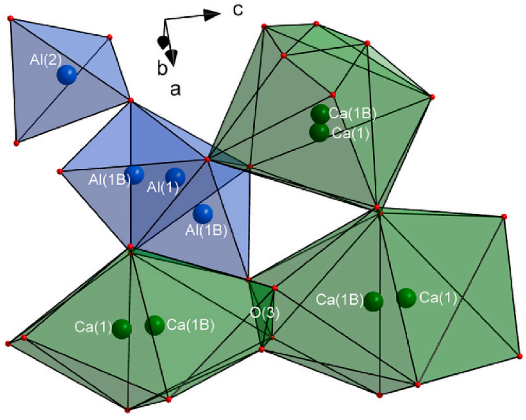

Fig. 1. Section of refined crystal structure obtained for the C12A7:Ni single crystal from SCXRD for illustration of split crystallographic sites and coordination polyhedra.

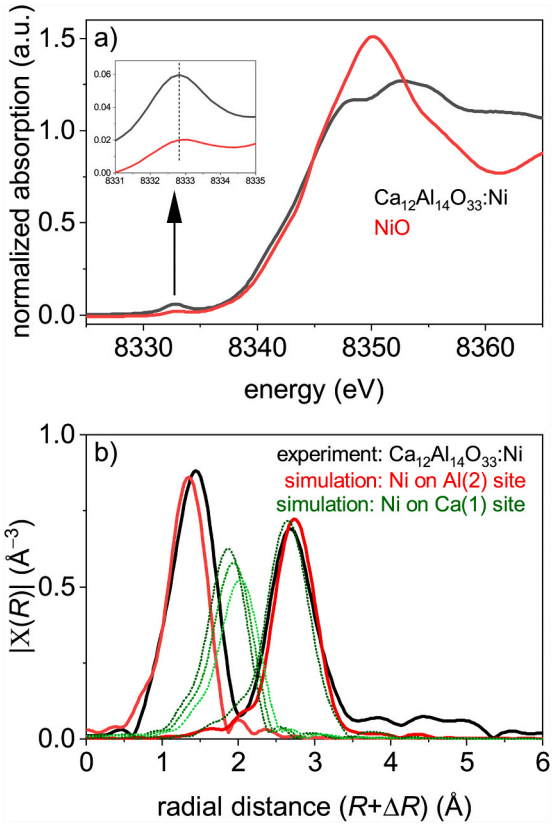

Fig. 2. a) Ni K edge XANES data obtained for the C12A7:Ni crystal and for a NiO powder reference material. b) FT of the k^2 weighted EXAFS oscillations empirically measured for the C12A7:Ni sample and simulated from SCXRD with Ni substituting either on the Al(2) or the Ca(1) site (see Table S3).

FTs with the simulations, it can be concluded that Ni substitutes Al on (distorted) tetrahedrally oxygen coordinated sites in C12A7:Ni. This is also in agreement with the fact that the ionic radius of Ni^{2+} (0.69 Å in 4-fold coordination) is much closer to that of Al^{3+} (0.53 Å in 4-fold coordination) than that of Ca^{2+} (1.14 Å in 6-fold coordination) [30] and also with the results from other works were the Al is reported to be partially substituted by iron [11]. Under the reasonable assumption that Ca is present as Ca^{2+} and Al as Al^{3+}, a substitution of an Al^{3+} by a Ni^{2+} would produce one (relative) negative charge that would need to be compensated by the release of 0.5 O^{2-} from the lattice. The substitution of only 0.068(2) Al^{3+} by Ni^{2+} per formula unit would consequently be accompanied by an oxygen deficiency of only $\delta_S \approx 0.034$ that is small

compared with $\delta \approx 0.25$ as suggested by the results from SCXRD, where the existence of the 33rd oxygen can only be determined with some uncertainty.

3.4. UV-VIS

Pure mayenite single crystals are transparent for visible light [10,11]. In most stable binary and ternary Ni-containing oxides nickel is present as Ni^{2+} and occupies octahedrally coordinated sites resulting in yellow or green colour appearance [31]. Ni^{2+} can (partially) be substituted also on tetrahedrally coordinated sites as reported for garnet [32] and hibonet [33] host structures for instance. The non-centrosymmetric tetrahedral oxygen coordination usually results in a blue/turquoise colour appearance. The transition from the ground state $^3T_1$ (^3F) to the $^3T_1$ (^3P) excited state here dominates the absorption characteristics from low energy red colour light to high energy green colour light [33]. Fig. 3 presents the UV-VIS absorption spectrum obtained for the C12A7:Ni crystal in reflection geometry. The excited $^3T_1$ (^3P) is split into the $^3A_2$ (^3P) and ^3E (^3P) state and creates an absorption gap for green light from about 2.16 to 2.26 eV. This strong state splitting can be explained by the (quasi) trigonal point symmetry reduction from T_d to C_{3v} that is most prominently realized for the Al(1B) and to somewhat smaller extend also for the Al(1) crystallographic site and as a consequence, the C12A7:Ni crystal has a green (also reported in Ref. [10]) and not a blue colour appearance. The partial substitution of the (quasi) trigonal Al(1) and/or Al(1B) site by Ni^{2+} is also in agreement with the results from DC magnetometry discussed below.

3.5. Magnetic characterization

The magnetometry data were corrected for diamagnetic contributions and the molar quantities were normalized to the Ni content according to the average composition $Ca_{12.045}Al_{13.887}Ni_{0.068}O_{33}$ (Table S2). As presented in Fig. 4, the field scans up to 9 T at 13 different temperatures ranging from 1.8 to 300 K as well as the temperature scan from 1.8 to 300 K at 9 T can very well be described by a magnetic model based on a phenomenological Hamiltonian that makes use of the *T–P* isomorphism to simplify the calculations of a many *d* electron system in a crystal field as outlined in Refs. [34,35] (see equations A1-4 as listed in Appendix A for the description of the Hamiltonian). According to the XAS results, Ni is present as Ni^{2+} on basically tetrahedral sites in C12A7:Ni. Ni^{2+} has an $[Ar]d^8$ electronic configuration with two unpaired electrons forming a total spin $S = 1$ and a ^3F term as free-ion ground state. ^3P is the first excited term with same multiplicity. In an ideal tetrahedron, the ^3F term splits into a $^3T_1$ ground state and the excited $^3T_2$ and $^3A_2$ states, and the ^3P term transforms into a $^3T_1$ state. The $^3T_1$ (^3F) allows for an orbital momentum contribution that might even be enhanced by admixture of the isosymmetric $^3T_1$ (^3P) state. In contrast, for an $[Ar]d^8$ configuration in an octahedral crystal field with $^3A_2$ ground state, the orbital momentum would be quenched. Applying the *T–P* isomorphism (in which the introduced triplet *P* term with effective $L = 1$ and $m_L = -1, 0, +1$ quantum mechanically mimics the three-fold degenerate triplet *T* state), the corresponding model C12A7:Ni consists of a spin $S = 1$ that is coupled to an effective orbital momentum $L = 1$ via a spin orbit coupling (SOC) constant λ_{SOC}. The orbital momentum is modified by an orbital reduction parameter $\sigma_{OR} = -A \cdot \kappa$ that accounts for effective orbital angular momentum due to covalency or low symmetry via the empirical constant $0 < \kappa < 1$. The prefactor *A* attributes to the *T–P* isomorphism and equals $^3/_2$ when representing a T_1 state as in the present case. Note that σ_{OR} in the applied model represents a parameter with some 'scaling properties', i.e. small deviations in the real Ni concentration might affect this parameter and a quantitative evaluation should therefore be considered critically, especially in the given case with low Ni concentrations. Trigonal distortions of a tetrahedral coordination (as present for the Al(1) and Al(1B) sites) would cause a splitting of *T* into a doubly degenerated *E* and a non-degenerate *A* state (see also UV-VIS results), whereas triclinic distortions would cause a further splitting into three non-degenerate *A* states. Within the framework of the *T–P* isomorphism, the crystal field parameter (CFP) B_0^2 is capable to reduce the point symmetry from tetrahedral to trigonal and the CFP B_2^2 further reduces the point symmetry to monoclinic/triclinic. The CFPs B_0^2 and B_2^2 are quantum formal analogues to the phenomenological axial and transverse zero field splitting (ZFS) parameters *D* and *E*, respectively. Since very good fits could be obtained for C12A7:Ni by including only B_0^2 in the model, B_2^2 was set to zero to avoid over parametrization. Note that the SOC constant λ_{SOC} is negative and the orbital reduction parameter σ_{OR} as applied for the *T–P* isomorphism is also negative what finally results in an effective $J = 0$ ground state with the higher *J*-multiplets representing excited states. In contrast, an $[Ar]d^8$ configuration of a free Ni^{2+} ion would exhibit a total orbital momentum of $L = 3$ that couples with the total spin $S = 1$ to form a $J = 4$ ground state.

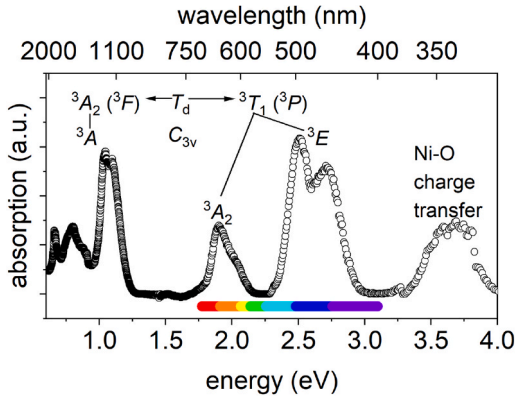

Fig. 3. Section of UV-VIS spectrum for the C12A7:Ni crystal measured in reflection. The absorption peaks correspond to electronic transitions and the final states are given for an ideal tetrahedral T_d and for a trigonal distorted C_{3v} point symmetry that describes the coordination of the Ni^{2+} within the mayenite host.

The fits of the applied model to the experimental data are shown in Fig. 4 and the obtained refined parameters are listed in Table 4. For illustrative reasons the simulations are plotted up to 15 T for the field scans and up to 500 K for the temperature scans. At 9 T and 1.8 K a free spin $S = 1$ would saturate at 2 μ_B and with an additional non-coupled $L = 1$ even at 3 μ_B. In contrast the experimentally observed value is strongly reduced to about 0.7 μ_B (Fig. 4a). As shown by the plot of the magnetic moment vs. reduced field $\mu_0 H \cdot T$ in Fig. 4b strong deviations from a pure Brillouin-type saturation behaviour of a free-ion are present visible by the not superimposing experimental curves. The progression of χT vs. temperature (Fig. 4c) is characteristic for a spin-orbit coupled system with effective positive spin-orbit coupling that has a quasi non-magnetic ground state ($J = 0$) with a local maximum at intermediate temperatures and slightly decreasing values for higher temperatures. The effective paramagnetic moment as extracted from an effective Curie constant $C_{eff}^{-1} = (\chi T)^{-1}$ is shown in the inset as a function of temperature (red line) with a maximum of about 3.61(1) μ_B at about 191 K. That is considerably higher than the spin only value of 2.83 μ_B for a spin $S = 1$ due to the orbital contributions stemming from excited high *J*-multiplets and still consistent with the range 2.8–3.5 μ_B as reported for typical experimental values for Ni^{2+} [36]. As shown in Fig. 4d, χ^{-1} exhibits a slightly bent progression over the whole temperature region due to the SOC interactions. This is an important feature that might lead to falsely extracted effective paramagnetic moments according to the Curie-Weiss law $C_{eff}^{-1} = d\chi^{-1}/dT$ that is only valid for paramagnetic systems with purely linear progression of χ^{-1} vs. temperature. The so determined effective paramagnetic moments (blue dashed line in inset of Fig. 4c) would further strongly depend on the specific temperature region

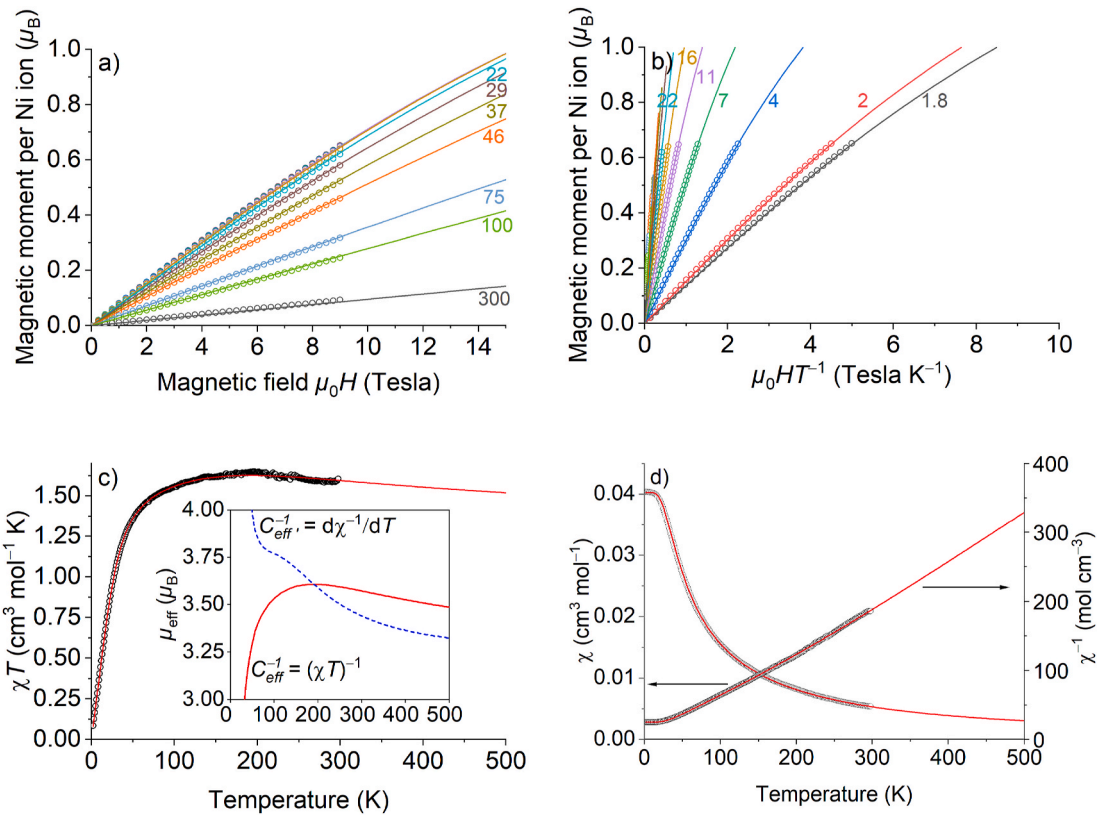

Fig. 4. Experimental DC magnetometry data measured for C12A7:Ni (circles) and fit curves according to the model described in the text (lines). a) Magnetic moment vs. field and b) magnetic moment vs. reduced field (numbers give temperature in K), c) χT vs. temperature with effective paramagnetic moment μ_{eff} determined via two different methods, and d) χ and χ^{-1} vs. temperature.

Table 4
Refined parameters obtained from a fit of the applied magnetic model (see text for details) to experimental DC magnetometry data measured for C12A7:Ni.

Parameter	
quantum numbers (fixed)	effective $L = 1$ and $S = 1$
CFP B_2^0 (cm^{-1})	69.5(2)
orbital reduction parameter σ_{OR}	−1.1253(6)
spin-orbit coupling λ_{SOC} (cm^{-1})	−98.11(8)
fit residual	0.11449(1)·10^{-3}

chosen for an actually non-valid Curie-Weiss fit. The magnetic properties of the Ni^{2+} in C12A7:Ni are not only characterized by a strong orbital contribution ($|\sigma_{OR}|$ slightly larger than one), but also by the accompanying axial anisotropy as parametrized by $B_0^2 = 69.5(2)$ cm^{-1} that is identical to a zero-field level splitting of the effective m_L states within the *T*–*P* isomorphism. Therefore, a reduction from tetrahedral to trigonal point group symmetry of the magnetic Ni center in C12A7:Ni is clearly found. This indicates that Ni is preferably positioned on Al(1) sites with trigonal oxygen coordination or on the even more distorted Al (1B) sites with quasi-trigonal symmetry. Since $B_0^2 > 0$ the non-magnetic effective $m_L = 0$ state is lower in energy compared to the effective $m_L = \pm 1$states, i.e. an easy-plane rather than an easy-axis anisotropy is realized. The easy-plane anisotropy together with the tetrahedral crystal field symmetry is most likely responsible for the observation that the magnetization vs. field curves measured at 1.8 K (Fig. S5) do not strongly depend on whether the crystal is measured in parallel orientation or in a 45° rotated orientation (see Fig. S2b). The magnetic properties found here are very different from those observed for a $Ca_{12}Al_{14}O_{33}$ single crystal with 1 at.% Al substituted by Fe [11]. Therein the authors find a linear progression of inverse susceptibility over the whole temperature range (down to about 5 K) and a very low Weiss constant T_W between −2 and −0.5 K, i.e. a quasi-free ion behaviour. The iron is reported to be present as Fe^{3+} in high spin configuration with $S = {}^5/_2$. Fe^{3+} has a ^6S ground state without any first order orbital contribution both as a free ion as well as within a crystal field.

3.6. Heat capacity

Fig. 5 shows the experimental isobaric molar heat capacity c_p vs. temperature plot that is fitted with a Debye-Einstein function

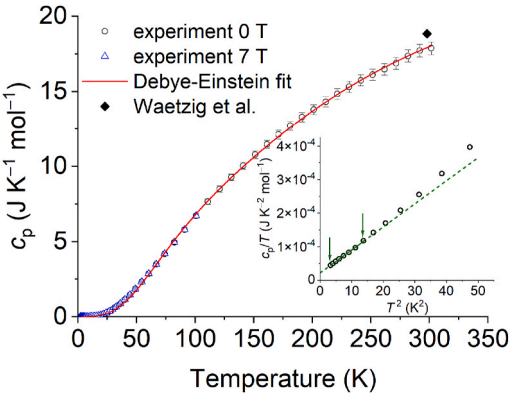

Fig. 5. Isobaric molar heat capacity c_p vs. temperature for the C12A7:Ni crystal at 0 and 7 T together with a Debye-Einstein fit. Inset: c_p/T vs T^2 plot together with linear fit (solid line) in the range between arrowsthe according to $c_p/T = \gamma + \beta \cdot T^2$.

$$c_p(T) \simeq c_V(T) = S_D \cdot 9R\left(\frac{T}{T_D}\right)^3 \int_0^{\frac{T_D}{T}} \frac{x^4 \bullet \exp(x)}{(\exp(x)-1)^2} dx + (1-S_D)\cdot 3R\left(\frac{T}{T_E}\right) \frac{\exp\left(\frac{T_E}{T}\right)}{\left(\exp\left(\frac{T_E}{T}\right)-1\right)^2} \quad (2)$$

with isovolumetric molar heat capacity c_v, Debye temperature T_D, Einstein temperature T_E, Debye-Einstein ratio S_D and gas constant R. For the specific molar heat capacity, the amount (given in units of mol) refers to the number of individual atoms within the measured sample and not the number of formula units (as used so far). There are 59 atoms (26 metal ions plus 33 oxygen ions) contained per formula unit. As molar mass for one formula unit the results for average composition from ICP-OES were used (Table S2). At 301(1) K a molar heat capacity of $c_p = 17.9(4)$ J K^{-1} mol^{-1} is measured that is still significantly below the Dulong-Petit value of 3 R = 24.9 J K^{-1} mol^{-1} that is supposed to be reached universally once all lattice vibration modes are excited. The best fit to the experimental data led to a Debye temperature of T_D = 406(4) K, an Einstein temperature T_E = 903(9) K and a Debye-Einstein ratio S_D = 0.45(8). The Einstein part of the heat capacity is ascribed to the optic phonon branch without a strong dispersion (constant energy) as compared with the acoustic phonons. Waetzig and Schilm [37] reported heat capacity values for a $[Ca_{12}Al_{14}O_{32}]^{2+}(2e^-)$ electride ceramic of 18.8 J K^{-1} mol^{-1} at 298 K (Fig. 5) and 25.9 J K^{-1} mol^{-1} at 1273 K. The value at 298 K is in good agreement with that obtained in this work and the reported evolution of the heat capacity from 298 to 1273 K confirms that the Dulong-Petit limit is reached at temperatures only far above room temperature. For temperatures well below the Debye temperature T_D and the Fermi temperature T_F the heat capacity of metals can be written as a sum of electron and phonon contributions that are linear and cubic in temperature, respectively: $c_p = \gamma \cdot T + \beta \cdot T^3$. Only in the very low temperature region the electronic contribution to heat capacity with a linear dependence on temperature is dominating over the phonon contribution with a cubic dependence on temperature. In the given case, a linear dependence of the c_p/T vs. T^2 plot was realized approximately from 1.8 to 3.7 K to (marked by arrows in the inset of Fig. 5) and a linear fit returned γ = 0.0218(8) mJ K^{-2} mol^{-1} and β = 6.9(1) μJ K^{-1} mol^{-1}. The γ parameter is two orders of magnitude lower than those for most metals with free electrons [38] indicating that there is negligible contribution from free electrons for C12A7:Ni, i.e. there are no indications for 'electride' properties.

3.7. Electric conductivity

The total resistivity of the C12A7:Ni sample (cross section $A = 0.513 \cdot 0.334$ cm^2 and thickness l = 0.072 cm) was above the device's limit of $R_{max} \geq 5$ GΩ at 300 K, i.e. the specific conductivity is lower than $\sigma_{min} \leq 8.40 \cdot 10^{-11} \Omega^{-1}$cm^{-1}. In Ref. [11] total electrical conductivity σ vs. temperature for single crystalline $Ca_{12}Al_{14}O_{33}$ with 1 at.% Al substituted by Fe and single crystalline [39] and polycrystalline [40] pure material are presented. They show approximately the same behaviour with the conductivity decreasing linearly from ~10^{-2} Ω^{-1} cm^{-1} at ~1000 °C to ~10^{-4} Ω^{-1} cm^{-1} at ~500 °C in a logarithmic plot of conductivity vs. inverse absolute temperature. A graphical extrapolation returns a hypothetical conductivity of ~10^{-6} Ω^{-1} cm^{-1} at 300 K. This is several orders of magnitude above the measured value for C12A7:Ni at 300 K, i.e. the oxygen anion mobility only contributes significantly to the total electrical conductivity at elevated temperatures above ~500 °C.

4. Conclusions

A mayenite single crystal containing a small amount of Ni was grown by the floating zone technique. The nickel content was determined by ICP-OES to be 0.068(2) per formular unit. The crystal structure was determined with SCXRD, and it could be confirmed that about 10 % of the Ca as well as the Al occupy additional distorted crystallographic sites. The presence of the 33rd cage oxygen anion connected to the disordered Al and Ca was also verified with some ambiguities due its very small general site occupancy. Despite the small Ni concentration, high quality X-ray absorption spectra were obtained at the Ni–K edge. It is indicated by XANES that Ni is present as Ni^{2+} in C12A7:Ni and the radial distribution function derived from EXAFS indicates that it occupies Al sites with basically tetrahedral oxygen coordination.

UV-VIS spectroscopy reveals that the excited $^3T_1$ (^3P) state is split into a $^3A_2$ (^3P) and a ^3E (^3P) state due to the (quasi) trigonal point symmetry reduction from T_d to C_{3v} that is most prominently realized for the Al(1B) position and to a smaller extend also for the Al(1) site. These findings are in agreement with the results from DC magnetometry. A magnetic model (phenomenological Hamiltonian) making use of the T–P isomorphism was found to explain the field scans at 13 temperatures from 1.8 to 300 K at fields up to 9 T as well as the temperature scan from 1.8 to 300 K very well. Accordingly, Ni is present as Ni^{2+} with spin quantum number $S = 1$ that is coupled to an effective orbital momentum $L = 1$ with $|\sigma_{OR}| = 1.1253(6)$ via spin-orbit coupling $\lambda_{SOC} = -98.11(8)$ cm^{-1}. The strong spin-orbit coupling easily explains the typical χT vs. temperature progression with a local maximum at about 191 K (with effective paramagnetic moment of 3.61(1) μ_B compared to 2.83 for a pure spin $S = 1$ system) and a very strong reduction at low temperatures. According to the refined axial crystal field parameter the tetrahedral oxygen coordination is trigonally distorted causing the T term (ideal tetrahedron) to be split into a double-degenerate E and a non-degenerate A state. As a consequence, Ni^{2+} is found to substitute Al on the Al(1) and/or Al(1B) site. Whereas the Al(1) site is characterized by a trigonally distorted tetrahedral oxygen coordination, the Al(1B) site has a pseudo-trigonally distored tetrahedral oxygen coordination where one center metal to oxygen distance is significantly larger compared to the three other non-equal metal to oxygen distances (see also Table 3).

The observed strong effects due to spin-orbit coupling and anisotropy on the magnetic properties are in strong contrast to what is reported for $Ca_{12}Al_{14}O_{33}$ with 1 at.% Al substituted by Fe^{3+} that behaves free-ion like without any significant orbital contribution and anisotropies due to the missing first order orbital momentum. The heat capacity and electric conductivity measurements reproduce well the results obtained for other pure/unsubstituted and non-electride mayenites.

Credit author statement

B.S.: conceptualization, methodology (magnetic models), investigation & formal analysis & validation & visualization: XAS, DC magnetometry, physical properties, and UV-VIS, writing - original draft S.E.: writing & discussions & editing A.E.: investigation & formal analysis & validation & writing - original draft: SCXRD, investigation: UV-VIS L.S.: investigation & formal analysis: XAS H.K.: crystal synthesis & investigation T.B.: investigation & formal analysis & validation: ICP-OES S.I.: writing – review & editing J.J.: writing – review & editing H.E.: writing – review & editing.

Declaration of competing interest

The authors declare that they have no known competing financial interests or personal relationships that could have appeared to influence the work reported in this paper.

Data availability

Data will be made available on request.

Acknowledgements

The XAS experiments were performed at CLAESS beamline at ALBA Synchrotron with the collaboration of ALBA staff.

Appendix A. Supplementary data

Supplementary data to this article can be found online at https://doi.org/10.1016/j.physb.2023.415090.

Appendix A

$$\widehat{H} = \widehat{H}_{SO} + \widehat{H}_{CF} + \widehat{H}_{ZEE} \tag{A 1}$$

Hamilton operator for spin-orbit coupling (SO), crystal-field interaction (CF) and Zeeman effect (ZEE).

$$\widehat{H}_{SO} = \sum_{i=1}^{N} \lambda_i \left(\sigma_{SO,i} \vec{\widehat{L}}_i \bullet \vec{\widehat{S}}_i \right) \tag{A 2}$$

Spin-orbit coupling constants λ_i, orbital-reduction parameters $\sigma_{SO,i}$, vector operator total orbital momentum $\vec{\widehat{L}}_i$, vector operator total spin orbital momentum $\vec{\widehat{S}}_i$.

$$\widehat{H}_{CF} = \sum_{i=1}^{N} \sum_{k=2,4,6} \sum_{q=-k}^{k} \sigma_i^k B_{ki}^q \theta_k \widehat{O}_{ki}^q \tag{A 3}$$

Crystal-field parameters B_{ki}^q ($A_{ki}^q \langle r^k \rangle_i$ in Steven's notation), operator equivalent factors θ_k and operator equivalents $\widehat{O}_{ki}^q$.

$$\widehat{H}_{ZEE} = \mu_B \sum_{i=1}^{N} \left(\sigma_i \vec{\widehat{L}}_i \bullet \overline{\overline{I}} + \vec{\widehat{S}}_i \bullet \overline{\overline{g}}_i \right) \bullet \vec{B} \tag{A 4}$$

with Bohr magneton μ_B, identity matrix I, g-tensor g_i and magnetic induction $\vec{B}$.

References

[1] J. Jeevaratnam, F.P. Glasser, L.S.D. Glasser, Anion substitution and structure of $12CaO{\cdot}7Al_2O_3$, J. Am. Ceram. Soc. 47 (1964) 105–106, https://doi.org/10.1111/j.1151-2916.1964.tb15669.x.

[2] K. Hayashi, M. Hirano, H. Hosono, Thermodynamics and kinetics of hydroxide ion formation in $12CaO{\cdot}7Al_2O_3$, J. Phys. Chem. B 109 (2005) 11900–11906, https://doi.org/10.1021/jp050807j.

[3] K. Hayashi, M. Hirano, S. Matsuishi, H. Hosono, Microporous crystal $12CaO{\cdot}7Al_2O_3$ encaging abundant O^- radicals, J. Am. Chem. Soc. 124 (2002) 738–739, https://doi.org/10.1021/ja016112n.

[4] K. Hayashi, S. Matsuishi, T. Kamiya, M. Hirano, H. Hosono, Light-induced conversion of an insulating refractory oxide into a persistent electronic conductor, Nature 419 (2002) 462–465, https://doi.org/10.1038/nature01053.

[5] S. Matsuishi, T. Nomura, M. Hirano, K. Kodama, S. Shamoto, H. Hosono, Direct Synthesis of Powdery Inorganic Electride $[Ca_{24}Al_{28}O_{64}]^{4+}(e^-)_4$ and Determination of Oxygen Stoichiometry, Chem. Mater. 21 (2009) 2589–2591, https://doi.org/10.1021/cm9007987.

[6] J. Irvine, A. West, $Ca_{12}Al_{14}O_{33}$ solid electrolytes doped with zinc and phosphorus, Solid State Ionics 40–41 (1990) 896–899, https://doi.org/10.1016/0167-2738(90)90147-J.

[7] M.I. Bertoni, T.O. Mason, J.E. Medvedeva, Y. Wang, A.J. Freeman, K. R. Poeppelmeier, Enhanced electronic conductivity in Si-substituted calcium aluminate, J. Appl. Phys. 102 (2007), 113704, https://doi.org/10.1063/1.2817605.

[8] S. Maurelli, M. Ruszak, S. Witkowski, P. Pietrzyk, M. Chiesa, Z. Sojka, Spectroscopic CW-EPR and HYSCORE investigations of Cu^{2+} and O^{2-} species in copper doped nanoporous calcium aluminate ($12CaO{\cdot}7Al_2O_3$), Phys. Chem. Chem. Phys. 12 (2010), 10933, https://doi.org/10.1039/c0cp00084a.

[9] K. Kurashige, Y. Toda, S. Matstuishi, K. Hayashi, M. Hirano, H. Hosono, Czochralski growth of $12CaO{\cdot}7Al_2O_3$ crystals, Cryst. Growth Des. 6 (2006) 1602–1605, https://doi.org/10.1021/cg0600290.

[10] M. Teusner, R.A. de Souza, H. Krause, S.G. Ebbinghaus, M. Martin, Oxygen transport in undoped and doped mayenite, Solid State Ionics 284 (2016) 25–27, https://doi.org/10.1016/j.ssi.2015.11.024.

[11] S.G. Ebbinghaus, H. Krause, D.-K. Lee, J. Janek, Single crystals of C12A7 ($Ca_{12}Al_{14}O_{33}$) substituted with 1 mol % iron, Cryst. Growth Des. 14 (2014) 2240–2245, https://doi.org/10.1021/cg401823k.

[12] S.G. Ebbinghaus, H. Krause, F. Syrowatka, Floating zone growth of large and defect-free Ca 12 Al 14 O 33 single crystals, Cryst. Growth Des. 13 (2013) 2990–2994, https://doi.org/10.1021/cg400406t.

[13] J. Koziskova, F. Hahn, J. Richter, J. Kožíšek, Comparison of different absorption corrections on the model structure of tetrakis(μ_2-acetato)-diaqua-di-copper(II), Acta Chim. Slovaca 9 (2016) 136–140, https://doi.org/10.1515/acs-2016-0023.

[14] O.V. Dolomanov, L.J. Bourhis, R.J. Gildea, J.A.K. Howard, H. Puschmann, OLEX2 a complete structure solution, refinement and analysis program, J. Appl. Crystallogr. 42 (2009) 339–341, https://doi.org/10.1107/S0021889808042726.

[15] G.M. Sheldrick, Shelxt – integrated space-group and crystal-structure determination, Acta Crystallographica Section A Foundations and Advances 71 (2015) 3–8, https://doi.org/10.1107/S2053273314026370.

[16] G.M. Sheldrick, Crystal structure refinement with SHELXL, Acta Crystallographica Section C Structural Chemistry 71 (2015) 3–8, https://doi.org/10.1107/S2053229614024218.

[17] K. Brandenburg, Diamond Version 2.1d, Crystal Impact GbR.

[18] L. Simonelli, C. Marini, W. Olszewski, M. vila Prez, N. Ramanan, G. Guilera, V. Cuartero, K. Klementiev, CLSS: the hard X-ray absorption beamline of the ALBA CELLS synchrotron, Cogent Physics 3 (2016), 1231987, https://doi.org/10.1080/23311940.2016.1231987.

[19] B. Ravel, M. Newville, ATHENA ARTEMIS HEPHAESTUS data analysis for X-ray absorption spectroscopy using IFEFFIT, J. Synchrotron Radiat. 12 (2005) 537–541, https://doi.org/10.1107/S0909049505012719.

[20] H. Lueken, Magnetochemie. Eine Einführung in Theorie und Anwendung, Teubner Studienbücher Chemie (TSBC), 1999.

[21] N.F. Chilton, R.P. Anderson, L.D. Turner, A. Soncini, K.S. Murray, PHI: a powerful new program for the analysis of anisotropic monomeric and exchange-coupled polynuclear *d*- and *f*-block complexes, J. Comput. Chem. 34 (2013) 1164–1175, https://doi.org/10.1002/jcc.23234.

[22] S.G. Ebbinghaus, H. Krause, F. Syrowatka, Floating zone growth of large and defect-free $Ca_{12}Al_{14}O_{33}$ single crystals, Cryst. Growth Des. 13 (2013) 2990–2994, https://doi.org/10.1021/cg400406t.

[23] H. Bartl, T. Scheller, Zur Struktur des $12CaO{\cdot}7Al_2O_3$, Neues Jahrbuch Mineral. Monatsh. 1970 (1970) 547–552.

[24] T. Sakakura, K. Tanaka, Y. Takenaka, S. Matsuishi, H. Hosono, S. Kishimoto, Determination of the local structure of a cage with an oxygen ion in $Ca_{12}Al_{14}O_{33}$, Acta Crystallogr. Sect. B Struct. Sci. 67 (2011) 193–204, https://doi.org/10.1107/S0108768111005179.

[25] R. Kiyanagi, J. Richardson Jr., N. Sakamoto, M. Yoshimura, Free oxygen ions and cage deformation in the nanoporous material $12CaO{\cdot}7Al_2O_3$: a temperature-dependent neutron powder diffraction study, Solid State Ionics 179 (2008) 2365–2371, https://doi.org/10.1016/j.ssi.2008.09.026.

[26] H. Boysen, M. Lerch, A. Stys, A. Senyshyn, Structure and oxygen mobility in mayenite ($Ca_{12}Al_{14}O_{33}$): a high-temperature neutron powder diffraction study,

Acta Crystallogr. Sect. B Struct. Sci. 63 (2007) 675–682, https://doi.org/10.1107/S0108768107030005.
[27] L. Palacios, S. Bruque, M.A.G. Aranda, Structure of gallium-doped mayenite and its reduction behaviour, Phys. Status Solidi 245 (2008) 666–672, https://doi.org/10.1002/pssb.200743425.
[28] L. Palacios, Á.G. de La Torre, S. Bruque, J.L. García-Muñoz, S. García-Granda, D. Sheptyakov, M.A.G. Aranda, Crystal structures and in-situ formation study of mayenite electrides, Inorg. Chem. 46 (2007) 4167–4176, https://doi.org/10.1021/ic0700497.
[29] S. Sasaki, K. Fujino, Y. Takéuchi, X-ray determination of electron-density distributions in oxides, MgO, MnO, CoO, and NiO, and atomic scattering factors of their constituent atoms, Proc. Jpn. Acad., Ser. B 55 (1979) 43–48, https://doi.org/10.2183/PJAB.55.43.
[30] R.D. Shannon, C.T. Prewitt, Revised values of effective ionic radii, Acta Crystallogr. Sect. B Struct. Crystallogr. Cryst. Chem. 26 (1970) 1046–1048, https://doi.org/10.1107/S0567740870003576.
[31] G.R. Rossman, R.D. Shannon, R.K. Waring, Origin of the yellow color of complex nickel oxides, J. Solid State Chem. 39 (1981) 277–287, https://doi.org/10.1016/0022-4596(81)90261-9.
[32] A. Bhim, S. Laha, J. Gopalakrishnan, S. Natarajan, Color tuning in garnet oxides: the role of tetrahedral coordination geometry for 3 *d* metal ions and ligand-metal charge transfer (Band-Gap manipulation), Chem. Asian J. 12 (2017) 2734–2743, https://doi.org/10.1002/asia.201701040.
[33] G. Costa, M.J. Ribeiro, W. Hajjaji, M.P. Seabra, J.A. Labrincha, M. Dondi, G. Cruciani, Ni-doped hibonite ($CaAl_{12}O_{19}$): a new turquoise blue ceramic pigment, J. Eur. Ceram. Soc. 29 (2009) 2671–2678, https://doi.org/10.1016/j.jeurceramsoc.2009.04.001.
[34] F. Lloret, M. Julve, J. Cano, R. Ruiz-García, E. Pardo, Magnetic properties of six-coordinated high-spin cobalt(II) complexes: theoretical background and its application, Inorg. Chim. Acta. 361 (2008) 3432–3445, https://doi.org/10.1016/j.ica.2008.03.114.
[35] M.E. Lines, Orbital angular momentum in the theory of paramagnetic clusters, J. Chem. Phys. 55 (1971) 2977–2984, https://doi.org/10.1063/1.1676524.
[36] A. Weiss, H. Witte, Magnetochemie, Grundlagen und Anwendungen, Verlag Chemie, Weinheim/Bergstrasse, 1972.
[37] K. Waetzig, J. Schilm, Electronic, mechanical, and thermal properties of $[Ca_{24}Al_{28}O_{64}]^{4+}(4e^{-})$ electride ceramic, International Journal of Ceramic Engineering & Science 3 (2021) 165–172, https://doi.org/10.1002/ces2.10098.
[38] C. Kittel, Introduction to Solid State Physics, John Wiley & Sons, Inc, EIGHTH EDI, 2005.
[39] D.-K. Lee, L. Kogel, S.G. Ebbinghaus, I. Valov, H.-D. Wiemhoefer, M. Lerch, J. Janek, Defect chemistry of the cage compound, $Ca_{12}Al_{14}O_{33-\delta}$—understanding the route from a solid electrolyte to a semiconductor and electride, Phys. Chem. Chem. Phys. 11 (2009) 3105, https://doi.org/10.1039/b818474g.
[40] M. Lacerda, J.T.S. Irvine, F.P. Glasser, A.R. West, High oxide ion conductivity in $Ca_{12}Al_{14}O_{33}$, Nature 332 (1988) 525–526, https://doi.org/10.1038/332525a0.